The University of New South Wales Extrasolar Planet Search: methods and first results from a field centred on NGC 6633

M. G. Hidas,[1][*] M. C. B. Ashley,[1] J. K. Webb,[1] M. Irwin,[2] A. Phillips,[1] H. Toyozumi,[1] A. Derekas,[1,3] J. L. Christiansen,[1] C. Nutto[1] and S. Crothers[1]

[1]*School of Physics, University of NSW, Sydney, NSW, 2052, Australia*
[2]*Institute of Astronomy, University of Cambridge, Madingley Road, Cambridge CB3 0HA*
[3]*School of Physics, University of Sydney, NSW, 2006, Australia*

ABSTRACT

We report on the current status of the University of New South Wales Extrasolar Planet Search project, giving details of the methods we use to obtain millimagnitude precision photometry using the 0.5-m Automated Patrol Telescope. We use a novel observing technique to optimally broaden the point spread function and thus largely eliminate photometric noise due to intrapixel sensitivity variations on the CCD. We have observed eight crowded Galactic fields using this technique during 2003 and 2004. Our analysis of the first of these fields (centred on the open cluster NGC 6633) has yielded 49 variable stars and four shallow transit candidates. Follow-up observations of these candidates have identified them as eclipsing binary systems. We use a detailed simulation of our observations to estimate our sensitivity to short-period planets, and to select a new observing strategy to maximize the number of planets detected.

Key words: methods: data analysis – methods: observational – binaries: eclipsing – planetary systems – open clusters and associations: individual: NGC 6633.

1 INTRODUCTION

The detection of extrasolar giant planets via high-precision radial velocity (RV) measurements of dwarf stars in the Solar neighbourhood has been highly successful. Since the first detection (Mayor & Queloz 1995) over 100 planets have been found (e.g. Butler et al. 2003; Tinney et al. 2003; Pepe et al. 2004). About 20 per cent of these planets have periods of less than 10 d.[1] These 'hot Jupiters' have a significant probability ($\sim$10 per cent) of having an orbital inclination that causes them to transit their host star. This makes possible an efficient photometric method of detecting such planets. In recent years, a number of groups have begun photometric monitoring of large samples of stars, with the aim of detecting transiting hot Jupiters (see Horne 2003 for a list of projects). The first known transiting planet, HD 209458b, was found using the RV method (Charbonneau et al. 2000; Henry et al. 2000; Mazeh et al. 2000). Only in the past year have transit searches finally begun to bear fruit, yielding five planets from the Optical Gravitational Lensing Experiment (OGLE) survey (Udalski et al. 2002a,b,c, 2003; Konacki et al. 2003; Bouchy et al. 2004; Pont et al. 2004; Konacki et al. 2005), and the first confirmed detection by a small, wide-field telescope (Alonso et al. 2004).

Due to geometric and time-sampling considerations, the transit method has a lower probability of detecting a given planet around a star than the RV technique. However, a search for transiting planets has considerable advantages.

(i) A transit search can be performed with a large-format CCD on a wide-field telescope, and can therefore monitor a large sample ($\sim$10^4) of stars simultaneously. For planets with periods shorter than $\sim$10 d, this outweighs the low transit probability and makes a transit search potentially more efficient than an RV search, which necessarily targets fewer stars. Transit searches therefore have the capacity to build a larger sample of known close-in giant planets.

(ii) Measurements of RV variations in the host star yield most of the planet's orbital parameters, but only a minimum mass ($M_p \sin i$). For a transiting planet, the orbital inclination (i) can be estimated from the light curve (typically to within a few degrees), and therefore the actual mass of the planet can be measured.

(iii) The radius of the planet can be measured from a fit to the transit light curve (and an estimate of the host star's radius), and therefore the average density of the planet is known, providing an important constraint for models of its structure and composition.

(iv) Transit searches can be tailored to search for planets around stars in various environments, such as in open clusters (e.g. Mochejska et al. 2004; von Braun et al. 2005), globular clusters (e.g. Gilliland et al. 2000; Weldrake et al. 2005), or in the Galactic disc.

---

[*]E-mail: mgh@phys.unsw.edu.au
[1] See http://www.obspm.fr/encycl/catalog.html.

RV searches need to target relatively bright stars, and are therefore better suited to searching for planets in the Solar neighbourhood.

(v) With ultrahigh-precision photometry ($\lesssim$0.1 mmag), transiting Earth-like planets may be found (e.g. Deeg 2002). These will be key targets for planned space missions such as the European Space Agency (ESA) *Eddington* (Roxburgh & Favata 2003) and the National Aeronautics and Space Administration (NASA) *Kepler* (Borucki et al. 2003).

(vi) Raymond, Quinn & Lunine (2004) have shown that terrestrial planets can form in the habitable zone (where liquid water can exist on the surface of a planet) of a star hosting a hot Jupiter. Assuming that the orbits in a planetary system are near co-planar, stars with known transiting hot Jupiters offer an excellent opportunity to detect (or rule out the existence of) terrestrial planets in the habitable zone.

(vii) While models suggest that planets may form and remain in stable orbits around binary stars (e.g. Artymowicz & Lubow 1994; Holman & Wiegert 1999), no circum-binary planets are known to date.[2] Such planets could be found by targeting known eclipsing binary systems, which offer an increased probability of a transiting configuration (if the orbits are co-planar), as well as the possibility of detecting non-transiting planets via precise timing of binary eclipses (Doyle & Deeg 2004, and references therein).

(viii) If the host star is sufficiently bright, the atmosphere of the planet can be studied using high-precision spectroscopy during a transit (e.g. Schneider 1994; Seager & Sasselov 2000; Brown 2001; Webb & Wormleaton 2001). To date, this has been done successfully for the planet orbiting HD 209458 (Charbonneau et al. 2002; Vidal-Madjar et al. 2003, 2004).

(ix) Infrared emission from a transiting planet may be detectable by the disappearance of spectral features when the planet is behind the host star (e.g. Richardson et al. 2003).

(x) Ultrahigh-precision photometry and timing of planetary transits have the potential to detect moons and rings around giant planets (e.g. Brown et al. 2001; Doyle & Deeg 2004; Barnes & Fortney 2004).

(xi) At a photometric precision of 10^{-5}, a transiting gas giant's oblateness can have a detectable effect on the light curve, placing constraints on the planet's rotation rate (Seager & Hui 2002). Lensing of the host star's light by the planet's atmosphere may also be detectable (Hui & Seager 2002), providing further information about its structure.

Transit searches ideally require a wide-field telescope, in order to monitor a large sample of relatively bright stars. Transiting planets around stars bright enough for high-resolution spectroscopic follow-up are the most valuable detections.

The other key ingredient is the ability to obtain high-precision photometry. A typical hot Jupiter (radius 1 R_{Jup}, orbiting a Sun-like star with a 3-d period) will cause a 1 per cent decrease in the host star's apparent brightness for $\sim$3 h. Therefore a transit search needs to achieve a relative photometric precision of a few mmag over time-scales of at least a few hours, which is a challenge for CCD photometry with a wide-field, ground-based telescope. The present paper is primarily concerned with the methods we have used to reach this precision, and the first results of our search.

In Section 2, we describe the Automated Patrol Telescope (APT) and the camera. In Section 3, we identify the major factors limiting

the photometric precision. The techniques we have used to overcome some of these limitations are discussed in Sections 4 and 5. In Section 6 we present the data we have obtained to date, the quality of the resulting light curves, and the first results from our search. Estimates of our expected detection rate in the current data, as well as for our improved observing strategy, are given in Section 7.

2 AUTOMATED PATROL TELESCOPE

The APT at Siding Spring Observatory (SSO), Australia, is owned and operated by the University of New South Wales (UNSW). It is a 0.5-m telescope of Baker–Nunn design, with a three-element correcting lens and an $f/1$ spherical primary mirror. It was originally used as a photographic satellite-tracking camera, before being donated to UNSW by the Smithsonian Institution, and converted for use with a CCD camera (Carter et al. 1992).

The camera was built by Wright Instruments, Enfield, UK. It uses an EEV CCD05-20 chip with 770×1150 (22.5 μm) pixel to image a 2×3 deg^2 field. However, the telescope has a potential field of view at least 5° in diameter, and a new camera is being built in 2005 to take advantage of this.

The telescope is housed in a building with a roll-off roof. The operation of the roof, the telescope and the CCD camera are all controlled via a PC running LINUX. An Internet connection to the PC gives a remote observer full control of the telescope. A local weather station and several web cameras allow the observer to monitor weather conditions and the operation of the telescope. The system also has the ability to close automatically in the event of rain, high humidity, or loss of connection to the Internet.

3 FACTORS LIMITING PHOTOMETRIC PRECISION

We have used simulated APT images to study the factors contributing to the photometric noise. Here we summarize only the most important factors for bright stars.

3.1 Poisson noise

For unweighted aperture photometry, the variance in flux due to Poisson noise is $\sigma_{\text{P,f}}^2 = (f + s)/g$, where f and s are the counts in the effective photometry aperture due to the star and sky, respectively ($\sigma_{\text{P,f}}$, f and s all in ADU), and g is the CCD gain ($g \approx 8\,\text{e}^-/\text{ADU}$ for the APT). Expressed as a root-mean-square (rms) variation in magnitude, provided $\sigma_{\text{P,f}} \ll f$, this becomes

$$\sigma_{\text{P}} = \frac{a}{f} \sqrt{\frac{f + s}{g}} \tag{1}$$

where $a = 2.5/\ln 10 \approx 1.086$, and the magnitude of the star is $m = z - 2.5 \log f$. The magnitude zero-point, z, is the magnitude of a star which results in one ADU of detected flux at zero airmass. For a 2.5-min APT image in the V band, $z \approx 22.5$. The precision we reach in practice is compared to this limit in Fig. 4.

3.2 Scintillation

Scintillation sets the theoretical minimum noise level for the brightest (unsaturated) stars. The magnitude scatter due to scintillation is given by (Kjeldsen & Frandsen 1992, equation 3)

$$\sigma_{\text{scint}} = (0.09\,\text{mag})D^{-2/3}\chi^{3/2}\Delta t^{-1/2}\text{e}^{-h/8}, \tag{2}$$

---

[2] With the possible exception of the system HD 202206, where the outer planet may have formed in a circum-binary disc around the primary and a brown dwarf companion (Correia et al. 2004).

where D is the telescope diameter in centimetres, χ is the airmass, Δt is the exposure time in seconds, and h is the altitude of the observatory in km. Using typical values for our observing programme with the APT ($D = 50$, $\chi = 1.5$, $\Delta t = 150$, $h = 1.1$), the estimated scintillation limit is 0.9 mmag rms per image.

3.3 Undersampling and intrapixel sensitivity variations

The CCD currently used in the APT camera has 9.43-arcsec pixels. The image of a star in the focal plane has a FWHM equivalent to only ~0.7 pixel (Toyozumi & Ashley, in preparation). It is far from a Gaussian profile, having a narrow, bright core, and broad, asymmetric wings (Fig. 2, left panel). This 'instrumental point spread function' (iPSF) is largely due to the telescope optics, and is therefore stable and largely independent of local seeing conditions. Its shape does however vary slightly with position on the CCD. When sampled by the CCD pixels, it becomes the 'effective PSF' (ePSF), with a width of ~1.0 pixel. For a focused star centred on a pixel, about 52 per cent of the light falls within that pixel.

Because of this severe undersampling, the effect of CCD intrapixel sensitivity variations (IPSVs) becomes important (e.g. Lauer 1999). Direct measurements by scanning the APT CCD with a small (<0.2 pixel) spot of light show that the point sensitivity varies by more than 30 per cent over a pixel in the V band (Toyozumi & Ashley 2005). As a result, the total flux detected for a star varies with its precise position within a pixel (Fig. 3, left panel). Combined with inevitable small shifts due to telescope jitter and differential refraction, this constitutes a significant source of photometric noise. Because IPSV is largely caused by the surface structure of the CCD, its amplitude decreases with increasing wavelength. For focused images, the detected flux varies by 4 per cent in the V band, and 2.5 per cent in the I band. As a result of the uniform structure of the CCD, the sensitivity variation is, to a good approximation, identical in all pixels.

Conventionally, PSF fitting is the technique of choice for general purpose precision photometry. However, with undersampling, IPSV and variation of the PSF over the field of view, photon-noise limited PSF fitting is extremely difficult to achieve. In principle, these effects can be accounted for, and practical methods for doing so have been described by Lauer (1999) and Anderson & King (2000). We have applied the algorithm of Anderson & King to APT images. While the the result was a significant improvement over naive aperture photometry, a precision below ~1 per cent could not be reached for most stars (Hidas et al. 2003, 2004). The severe undersampling of APT images is the likely cause of this limit. Most of the objects to be measured are blends of several unresolved stars. Thus, the true number of PSFs contributing to the observed pixel flux distribution is often significantly higher than what the model is fitting (or is capable of deriving from the image itself).

3.4 Flat-fielding

We have made sure that flat-fielding errors do not make any significant contribution to the photometric noise for bright stars. Any changes in the pixel-to-pixel sensitivity variations over time-scales of a few months are at a level below 0.1 per cent. We combine a sufficient number of twilight flat-field images so that the Poisson noise in the combined master flat is also well below 0.1 per cent rms per pixel.

Note that as twilight skies have generally bluer optical colours than dark skies, while most target stars generally have redder colours, the pixel response as a function of wavelength also needs
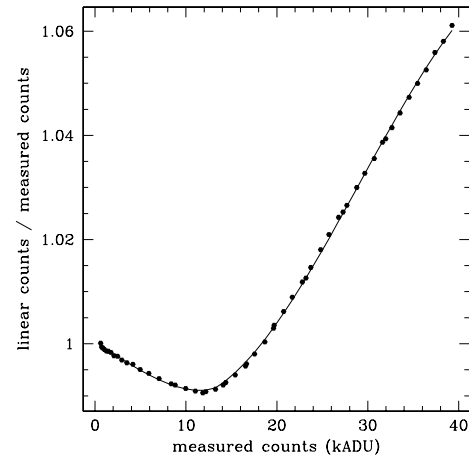

Figure 1. Deviation from linearity of the CCD response, measured from a set of dome flat images taken at a range of exposure times. The fitted curve (two third-order polynomials joined at ~13 000 ADU) is used to correct images for this effect.

to be taken into account. However, this is not a problem if only the overall sensitivity is dependent on wavelength, and the relative pixel-to-pixel differences are constant. This seems to be the case for most CCDs.

3.5 Non-linearity of CCD response

The relationship between the flux incident on the CCD and the resulting pixel values can be significantly non-linear, largely due to the CCD readout amplifier. This can be another limiting factor for precision differential photometry from undersampled images, where the distribution of pixel values in the photometry aperture can vary considerably from image to image.

Fig. 1 shows our measurement of the response of the APT CCD to a range of incident flux levels (in flat-field images). The signal in bright pixels deviates from linearity by up to 6 per cent, which is large compared to many CCD cameras. We have fitted two third-order polynomials (above and below 13 000 ADU) to these data, and use this fit to correct every image before further processing. As the residuals from the fit are less than 0.05 per cent, this correction reduces the effect of non-linearity on the photometric noise to below 0.5 mmag.

3.6 Crowding

In a crowded field, photometry apertures placed around stars frequently have relatively bright pixels near their boundaries. These are from blended or nearby stars within a distance of ~30 arcsec (the radius of the aperture we use). Small shifts in position (~1 pixel), due to telescope jitter and image rotation, cause variations in both the brightness of such pixels, and the extent of their overlap with the aperture. The amplitude of this additional noise will depend on each individual star's immediate neighbourhood in the field. In the worst case, the presence of a relatively bright neighbour can add 10–20 mmag (rms) of noise. This can occur for all stars, but will occur more commonly for the fainter stars.

Furthermore, the presence of faint, unresolved background stars makes the effective sky level more noisy and variable over short spatial scales. Thus, while crowding does not place a strict limit on

the precision, on average it increases the level of noise in the light curves.

In order to minimize the additional photometric noise due to crowding, we have experimented with allowing each object to have a different sized photometry aperture. The aperture radius is chosen to minimize the flux in the brightest pixel near the boundary in a sample image, while applying a weight towards smaller apertures. Once a radius is chosen for an object, it is kept fixed for all measurements. For most stars fainter than $V = 14.5$, this reduces the rms scatter by at least 20 per cent. To date, we have found no clear improvement for the brighter stars, although future refinement of this idea may lead to significant gains.

Besides contributing to the photometric noise, crowding has another important effect on our ability to detect variations in a star's magnitude (including transits). The additional light from blended stars 'dilutes' the amplitude of any variations, reducing the signal-to-noise (S/N) ratio of planetary transits, and making the eclipses of binary stars appear more like transits (see Section 5.5).

3.7 Atmospheric conditions

Relative photometry is generally not affected by temporal variations in overall sky transparency over the course of a night. However, the transparency can also vary spatially, for example due to undetected thin clouds. For a wide-field instrument such as the APT, this can result in significant variations in magnitude differences across the field, and thus additional noise in the relative photometry. When such 'non-photometric' conditions occur, they can degrade the precision for bright stars ($9 \lesssim V \lesssim 13$) to 5–10 mmag, making the data obtained only marginally useful.

3.8 Systematic errors

Systematic variations in apparent magnitude common to all stars are removed by calibrating the photometry using a large sample of stars (see Section 5.2). However, in some of the resulting light curves, systematic trends do remain. These are usually in the form of a linear change in apparent magnitude with time, amounting to a $\sim$10 mmag decrease or increase over the course of a night. We note that similar trends have been observed in light curves from other photometric surveys, such as HATNet (Bakos et al. 2004), MACHO (Drake & Cook 2004) and OGLE (Udalski et al. 2003), although the latter authors also claim that these can be removed using a method developed by Kruszewski & Semeniuk (2003).

In our own data, these systematics may be largely due to the inability of our sky fitting routine to accurately follow changes in the effective background signal over small spatial scales. This can occur in regions of the field where the density of faint, unresolved background stars is large (e.g. near the centre of an open cluster). Combined with the time-dependent slope in the intrinsic sky brightness, this can lead to the kind of trends we observe. We are working on an improved sky fitting algorithm in order to minimize these effects.

Small changes in the camera focus also lead to systematic errors in the relative photometry, as they alter the contribution of light to each star's photometry aperture from blended or nearby stars. Because the magnitude of this change varies depending on each star's immediate neighbourhood, it cannot be simply corrected for. While the focus is stable over the course of a typical observing run, it does need to be reset occasionally, in particular after a filter change. This effect can cause magnitude offsets from night to night in the light curves of some stars (those whose fractional contribution from
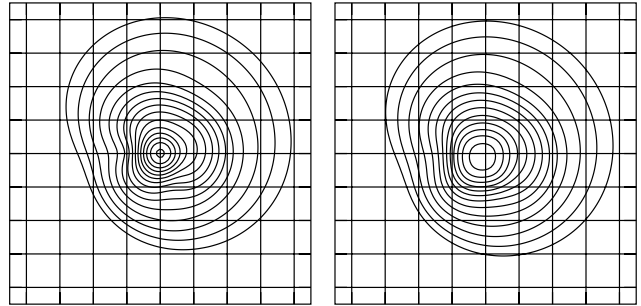

Figure 2. The iPSF of the APT near the centre of the field. Each PSF has been normalized to have a total flux of 1. The contour levels are identical in both panels, and have uniform logarithmic spacing. The grid spacing corresponds to one CCD pixel. Left panel: the normal, focused iPSF, determined by fitting a multiGaussian model to a set of 150-s, V-band images of a bright star (Toyozumi & Ashley, in preparation). The FWHM is $\sim$0.7 pixel and the peak intensity $\sim$1.1. Right panel: the broadened iPSF obtained by the raster-scan technique. This model was calculated by numerically convolving the normal iPSF with the raster-scan pattern followed by the telescope (Ashley et al., in preparation). It has a FWHM of $\sim$1.5 pixel, and a peak intensity $\sim$0.5.

neighbours is significantly different from the reference stars used for calibration).

4 OBSERVING STRATEGY

4.1 Raster-scan technique

Tests with severely defocused images (FWHM $\approx$ 10 pixel) have shown that a relative photometric precision of at least $\sim$3 mmag was possible with the APT, for bright ($V \approx 7$) stars in sparse fields. Of course, such images are not appropriate for observing a large number of fainter stars in crowded fields.

A new observing technique has allowed us to achieve the same precision without degrading image quality (Ashley et al., in preparation). During each exposure, the telescope is moved in a precise raster-like pattern covering the area of a single CCD pixel. This broadens the effective PSF only slightly (FWHM $\approx$ 1.5 pixel; see right panel of Fig. 2). However, because each point on the iPSF scans over a range of subpixel positions during the exposure, the sensitivity variations within the pixel are effectively averaged out (Fig. 3). Residual variations in the detected flux due to IPSV are limited to $\lesssim$1 mmag.

A slightly different technique, based on the same idea of broadening the PSF by moving the telescope during exposure is used by the Hungarian Automated Telescope (Bakos et al. 2004).

4.2 Nightly routine

Most of the observations are conducted remotely via the Internet. The observer's main task is to initiate the observing process, and to monitor weather conditions and the quality of the data obtained. Each of the tasks of starting up the telescope system, opening the roof, taking twilight flats, and the observations themselves are executed via simple shell scripts on the telescope-control PC.

Twilight flat-field images are taken on most clear evenings when the Moon is down, and on some mornings. $\sim$15 images with sufficiently high background flux can be taken per twilight. Other calibration images are not necessary for the APT camera. The bias
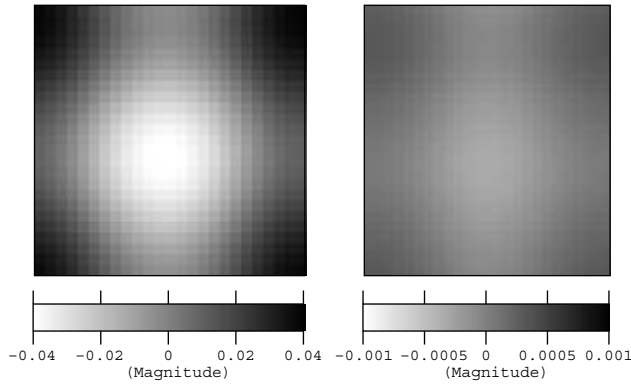
Figure 3. The effect of IPSVs on the photometry from undersampled images taken by the APT. Each image represents one CCD pixel, and shows the relative magnitude measured for a star, as a function of its position within the pixel. An accurate model of the iPSF, obtained from real images (Toyozumi & Ashley, in preparation), was convolved with the pixel sensitivity, as measured by scanning the CCD with a spot of light (Toyozumi & Ashley 2005). The two panels correspond to the two iPSF models presented in Fig. 2. Left panel: the result for normal, focused APT images in the *V* band. Right panel: the reduced effect when the PSF is broadened by the raster-scan technique (Section 4.1). Note the difference in scale.

level shows no significant structure over the CCD, and can be accurately measured from the overscan region. Dark current is negligible ($\sim$0.6 e$^-$ per pixel per second).

During the night, as each image is read out, an astrometry program locates Tycho-2 stars (Høg et al. 2000) in the image, and calculates the (linear) transformation from CCD pixel coordinates to celestial coordinates. The coefficients of the transformation are written to the FITS header as a world coordinate system (WCS). Typically, $\sim$200 Tycho-2 stars are matched. In this way, telescope pointing is kept accurate to within $\sim$0.2 of a pixel. This helps reduce the effects of any flat-fielding errors, as stars near the centre of the field are always imaged by the same pixels. As differential refraction by the atmosphere causes a gradual rotation ($\sim$4 arcmin in 8 h) and change in image scale ($<$0.1 per cent), stars near the corners of the field will shift by $\sim$1 pixel.

The astrometry program also performs a quick measurement of the magnitudes of the Tycho stars and compares them to the catalogue values. This allows the remote observer to monitor sky transparency and detect the presence of clouds.

For most of our 2003–2004 observations, the telescope continuously cycled between four adjacent fields, taking 150-s exposures, as long as the fields were observable. Including CCD readout and telescope slew time, each image took 3.5 min. On a full clear night $\sim$30 images per field were obtained. Due to physical limitations of the mount, the telescope can follow a field for a maximum of $\sim$8 h.

5 ANALYSIS STRATEGY

5.1 Data reduction

Optimal aperture photometry can be competitive with PSF fitting for moderately crowded fields (e.g. Naylor 1998). For brighter stars, variance-weighted PSF fitting is equivalent to standard aperture photometry (e.g. Irwin 1997). This and the constancy of the PSF for the APT have enabled us to develop a simple, robust and extremely accurate aperture photometry package for processing APT images.

Image crowding, usually the bugbear of aperture photometry, is dealt with in a novel, yet simple manner.

Briefly, each APT frame is processed in the standard manner up to and including generation of object catalogues using the development toolkit of the Isaac Newton Telescope (INT) Wide Field Survey (WFS) pipeline software (Irwin & Lewis 2001). Particular care is taken over flat-fielding, because we need to ensure the gross pixel-to-pixel sensitivity variations are mapped to better than the 0.1 per cent level. We combine all the twilight flats (of order 100) obtained during a 3–4 month season. Each twilight image has $\sim$20 000 counts (the gain is $\sim$8 e$^-$/ADU).

Non-linearity of pixel counts is dealt with by first measuring the global non-linearity from a varying time series of, essentially, flat-field frames under constant illumination and then applying the derived constant look-up-table correction to all pixels before processing.

The final stages of the INT WFS pipeline involves generating object catalogues for each frame. Among other things, the object catalogues are used to derive accurate six-parameter linear frame-to-frame transforms with respect to a chosen master reference frame. To date, a single, low-airmass image from a dark, photometric night has been chosen as the master frame for each field. In the future, a separate master image will be generated by stacking a dozen or so consecutive images. This will remove spurious objects from the master catalogue (such as cosmic rays), and improve the astrometric precision.

The transformations are of the general linear form

$$x' = ax + by + c, \qquad y' = dy + ex + f, \qquad (3)$$

where a and d define the relative x and y scales, b and e the rotation and/or shear, and c and f the global shifts. Note that we could perform these transformations using the WCS data stored in each image header. However, this would not make optimal use of the information in each frame (the WCS transformations are calculated using $\sim$200 Tycho stars, while the full object catalogues typically contain 10 000 objects to be matched to the master catalogue), and would limit the accuracy to $\sim$0.1 pixel.

Although we attempt to place the exposures of each target on comparable field centres within each night and from night to night by performing astrometry on each image as it is read out, small differential adjustments of the order of one pixel are still required. Even with apparently perfectly aligned images, small temperature changes throughout nights, differential refraction variations as a function of airmass and differential field rotation all contribute significant pixel level distortions. However, the approximate global alignment does ensure that non-linear terms are negligible at this pixel scale.

The reference frame catalogue also defines the master coordinate list to be used for the later analysis, and this is transformed (to within 0.01 of a pixel) on to each frame to be processed. Without this stage, relative accuracies of $\sim$0.1 of a pixel are still possible, from the individual image catalogues. However, with these undersampled images, coordinate accuracies of 0.1 pixel are not sufficient to give mmag photometry for the brighter objects. This is particularly important in crowded fields, where bright pixels on the boundary of the photometry aperture are frequent (see Section 3.6). Variations in the contribution to the aperture sum from these pixels due to errors in aperture centring need to be minimized. Tests have shown that errors of $\sim$0.1 pixel in the aperture positions increase the photometric noise by 50 per cent for the average bright ($V \lesssim 14$) star in a crowded field (compared to the near-photon-limited results we otherwise achieve).
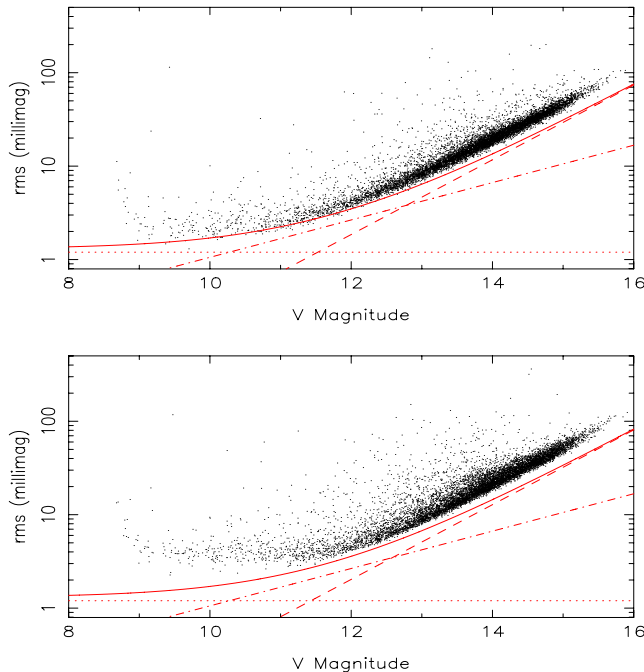
Figure 4. Photometric precision from one night (top panel) and five nights (bottom panel) of APT observations of the field centred on the open cluster NGC 6633 (2002 August). The solid line is the theoretical estimate, including Poisson noise in the star flux (dot-dashed) and sky flux (dashed), and a magnitude-independent term (dotted). The latter term (1.2 mmag) represents scintillation, as well as any residual errors due to flat-fielding, non-linearity and IPSV. Stars brighter than $V \approx 9$ are saturated in a 150-s APT image.

The final ingredient is a very stable and robust two-dimensional background estimator, which is used to estimate and remove the global background in a highly repeatable manner in each frame. With this kit of parts, each data set can be analysed in (almost) exactly the same way, using the same apertures accurately co-located on each frame. Each aperture sum includes subpixel partitioning of flux and the whole package runs completely automatically.

The main advantage of this approach is that systematics from crowding are the same in each frame because of the PSF stability and the differential coordinate precision, and even quite crowded fields can be successfully analysed because essentially identical image confusion arises in all cases. With this approach, we are achieving differential photometric precision of better than 2 mmag for bright objects and are close to the theoretical photon noise limit at all magnitudes (Fig. 4).

5.2 Photometric calibration

Global image-to-image magnitude variations are removed by ensemble relative photometry. An approximate magnitude zero-point (good to ~ 0.1 mag) is set by comparison with the magnitudes of 100–200 stars from the Tycho-2 catalogue. Stars in the range $9 < V < 11$ are then used for the calibration. There are typically ~ 1000 of these in a dense Galactic field. Magnitude residuals (Δm) from the nightly mean value for each reference star are calculated, and for each image, fitted by a function of the form

$$\Delta m = a + bx + cy + dxy + ey^2 \tag{4}$$

where x, y are the star's pixel coordinates on the CCD, and a–e are constants for an image. A second-order term in y was necessary

because the CCD is larger along the y-axis, which corresponds to the right-ascension direction (along which the airmass varies more). Adding an x^2 term to the fit does not significantly improve the photometric precision. Therefore, to make the fit more robust, this term is not included. As this function provides a good approximation to the variation in airmass across the field, a separate airmass term is not necessary.

This fit is then subtracted from each star's magnitude. Mean magnitudes and residuals are recalculated. Based on the rms residuals of each star over the night's data, variable and badly measured stars are removed from the reference list, and the whole process is repeated. In most cases, the coefficients of the fit are effectively zero after four to seven iterations. Any images for which the median rms of stars with $9 < V < 12.5$ remains higher than 15 mmag after calibration are rejected, and the calibration is repeated without them.

The above process is applied to each night's data separately. Any remaining night-to-night magnitude zero-point offsets are removed at the time the final light curves are compiled.

5.3 The pipeline

The entire data reduction process, from raw images to calibrated magnitudes, can be run automatically using a Perl script. The only interactive part of the procedure is the selection and combining of a suitable set of twilight flats to create a master flat-field image. This needs to be done once for each 3–4 month season of data. Running on a Sun Enterprise 4500 workstation (with eight CPUs and 4 Gb of memory), the pipeline will then process a full night's data in less than 2 h, and several of these processes can be run in parallel.

From each data set, two sets of magnitudes are generated, measured with photometry apertures two and three pixels in radius. The larger aperture gives a slightly lower average rms for most bright stars, but is more susceptible to contamination of light curves by close neighbours. When a small-amplitude signal, such as a transit, is found in a light curve, a comparison of the signal amplitude measured by the two apertures provides a quick way of identifying such contamination.

5.4 Candidate selection

Initially, we visually inspect the light curves for the brightest 2–3000 stars in each field (down to $V \approx 13$). This procedure has the advantage of being less susceptible to spurious detections due to variable stars and systematic errors than detection software.

We also use the transit detection algorithm described in Aigrain & Irwin (2004). Light curves are first searched for individual, box-shaped transit events of a given trial duration, and the S/N ratio of a transit at each trial epoch is stored. These S/N values are then used to perform a period search. This is repeated for a number of trial transit durations, and the combination of period, duration and starting epoch resulting in the highest total S/N (over all observed transits) is selected for each light curve. A number of selection criteria are applied, based on the individual transit and total S/N, as well as the distribution of S/N values (over all trial parameters) for each light curve.

To date, the effectiveness of this detection software has been limited by the presence of systematic trends in our light curves (see Section 3.8), which lead to frequent spurious detections. Kovács, Bakos & Noyes (2004) have recently published details of a trend filtering algorithm which substantially improves the quality of light curves obtained by the HATNet project (Bakos et al. 2004). Our

initial experiments applying this algorithm to APT data had promising results, although our implementation has yet to be refined. At present, it does greatly reduce the amplitude of systematics while preserving most transit signals, but also increases the white noise somewhat. We have not yet fully characterized the sensitivity of our detection software, but preliminary tests have shown that in the absence of systematics, 10 mmag transits are detected in a high percentage of cases (provided multiple transits are present and the total S/N is sufficiently high).

5.5 Eliminating false positives

Brown (2003) has estimated that up to ∼90 per cent of planet candidates selected by a wide-field transit search are binary stars. Grazing eclipses of binary stars, and eclipsing binaries with their light diluted by a third blended star can mimic the depth, and (to some extent) the shape of a planet transit. It is essential to eliminate these false positives at the earliest possible stage of the follow-up process. Our follow-up strategy is outlined below. At each stage we focus on the most promising planet candidates. Depending on the available observing time we also follow up likely binary systems.

(i) Inspection of a Digitized Sky Survey[3] image, to reveal how much blending is present in the APT image (our photometry apertures are effectively ∼1 arcmin in diameter, which is typical for wide-field transit search projects).

(ii) Estimation of the physical parameters of the system, in particular the radius of the transiting object, from the light curve. The light curve is parametrized by the period (P), transit depth (ΔF) and the durations of the complete transit and the 'flat bottom' part (t_T and t_F). From these, the primary star's density can be calculated (Seager & Mallén-Ornelas 2003). Assuming a stellar mass–radius relation then yields the primary's radius (R_1) and the radius of the transiting object $R_2 = R_1\sqrt{\Delta F}$. Assuming the transit is in front of the brightest star in the APT aperture and adjusting the transit depth accordingly gives a lower limit on the size of the transiting object.

(iii) Photometric monitoring of the target area at higher spatial resolution, during a predicted transit, to identify the host of the transiting object, and measure the true (or at least less diluted) transit depth. This is done in multiple colours so that the colour signature of a grazing or blended eclipsing binary can be detected.

(iv) Medium-resolution spectroscopic follow-up to identify the host star's spectral class, allowing a more precise estimate of its radius, and therefore the radius of the planet. The presence of double absorption (or emission) lines, features from different spectral types, and in particular large RV variations in phase with the transit signal, would indicate a binary or blend.

(v) For the best candidates, high-precision RV measurements (using echelle spectroscopy) will allow the measurement of the transiting object's mass and confirm or rule out its planetary nature.

6 RESULTS

6.1 Fields observed

We have targeted two groups of four adjacent fields, one group in Centaurus, the other in Ophiuchus. Both groups are within 10°

---

[3] The Digitized Sky Survey was produced at the Space Telescope Science Institute under US Government grant NAG W-2166, based on photographic data obtained using the Oschin Schmidt and UK Schmidt telescopes.
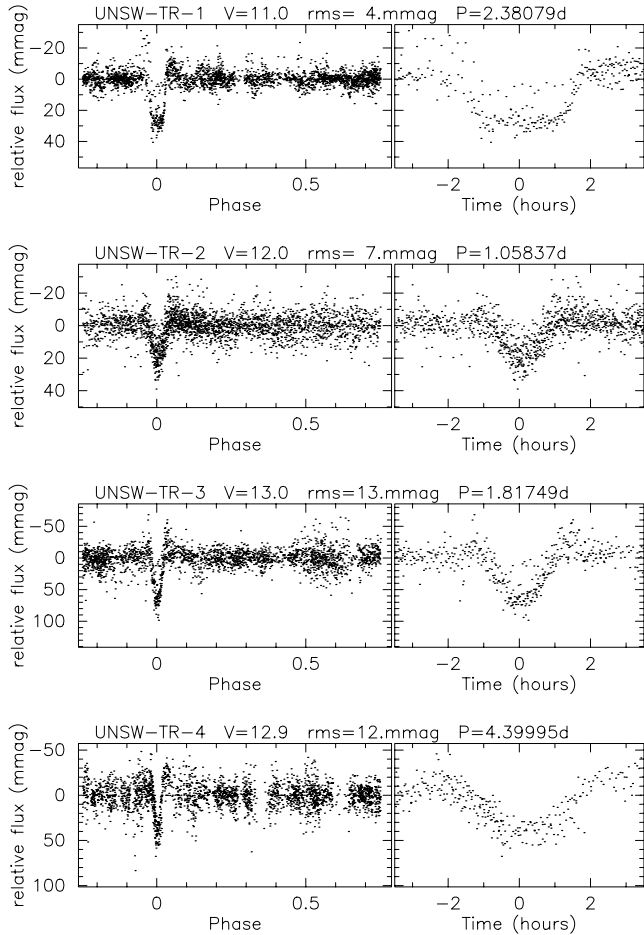
Table 1. Fields targeted in the UNSW planet search.

Field name	RA (J2000)	Dec. (J2000)	b	$N_*(V < 14)$	N_{nights}
NGC 3532	11^h 07^m	−58° 42′	1°	7000	61
G1	11^h 31^m	−58° 42′	3°	7000	65
G2	11^h 31^m	−56° 30′	5°	7000	60
G3	11^h 07^m	−56° 30′	4°	7000	59
NGC 6633	18^h 28^m	+6° 35′	8°	5000	79
H1	18^h 28^m	+4° 30′	7°	4000	47
H4	18^h 41^m	+4° 30′	4°	3000	30
H5	18^h 41^m	+6° 35′	5°	5000	30

of the Galactic plane. The field centres are shown in Table 1. We have centred one field in each group on an open cluster (NGC 3532 and 6633). However, as each cluster contains only a few hundred relatively bright stars (e.g. Koelbloed 1959; Jeffries 1997), and many of these are blended or saturated, only a small fraction of the stars we measure are cluster members.

We began observing most of these fields in 2003, and we now have two full seasons worth of data for each of them. The first observations using the method described in Section 4 were taken in 2002 August, targeting the open cluster NGC 6633 as part of a multisite campaign (Martín et al. 2004). A total of 690 images were taken through a Johnson V filter on eight consecutive nights (August 7–14). In 2003, we added the three adjacent fields, and obtained another 180 images of NGC 6633 in the V band (June) and 380 in the R band (July–August). During the 2004 season, we continued to observe the field in the V band (March–July, 1800 images), including some nights where we again observed this field only, to obtain higher-cadence measurements. About one-third of the images taken in 2004 (typically those taken in the first part of the night) were affected by a technical problem which has rendered them largely unusable. Finally, in August 2004 we began observing in the I band, and took 230 images of NGC 6633. For these latter observations, the exposure time was reduced to 60 s, as the CCD is more sensitive in this band.

Due to its northern declination, the NGC 6633 field can be observed for a maximum of 7 h at relatively low airmass. From experience, useful images can be taken up to an airmass of ∼2.2. The minimum airmass reached by this field is 1.3.

With a threshold of 4σ above the background, the pipeline software typically detects ∼9000 objects in the field, the faintest of these having $V \approx 15.5$. In each image, the positions of ∼7000 of these objects are matched to the master catalogue to obtain the coordinate transformations into that image, with mean residual errors of ∼0.05 pixel.

The relative photometric precision achieved on a single clear night, and over a week of observations, is shown in Fig. 4. For stars in the range $9 \lesssim V \lesssim 11$, we routinely achieve 2 mmag precision. For this field, the nightly rms is under 10 mmag for 2300 stars.

6.2 Transit candidates

The light curves for the brightest ∼2000 stars (down to $V \approx 13$) from the NGC 6633 field were searched for transit-like events by visual inspection. Through this process we identified four light curves with transits shallow enough (<100 mmag) to be considered as potential planet candidates. Their light curves are shown in Fig. 5.

Table 2 summarizes the properties of the candidates, including an estimate of the transiting object's minimum radius (see item ii under Section 5.5). With relatively large radii, our candidates

Figure 5. Phase-folded light curves of the four transit candidates found in the NGC 6633 field. The light curves include all *V*-band data of reasonable photometric quality (nightly rms $\lesssim$10 mmag and at least 10 points per night) we obtained during 2002–2004. Note that UNSW-TR-2 is folded at its originally estimated period. Follow-up observations have shown that this is a binary system with two nearly identical eclipses, and the true period is twice this value.

seemed unlikely to be planets. The largest extrasolar planet known to date (HD 209458b) has a radius of 1.35 $R_{\rm Jup}$ (Brown et al. 2001). However, as Drake & Cook (2004) point out, there are currently too few transiting objects with known mass to place a firm upper limit on the radii of extrasolar planets and brown dwarfs. Although not our primary targets, brown dwarfs and low-mass stellar objects may also yield interesting results. We also note that in the *V* band, neglecting the effects of limb darkening (as we have done for these
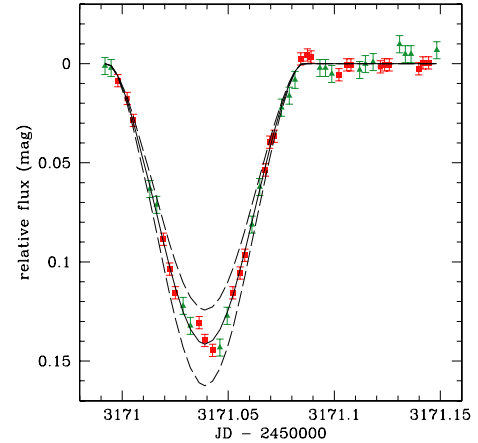

Figure 6. The undiluted eclipse signal from transit candidate UNSW-TR-2, observed at high spatial resolution with the 40-inch telescope at SSO. We observed a single transit, and alternated between *V* band (triangles) and *I* band (squares). The solid line is the model light curve for an eclipsing system consisting of two K7V stars (with masses 0.58 M$_\odot$ and radii 0.64 M$_\odot$) in a 2.12-d orbit, at an inclination of $\sim$83°. The dashed lines show the result of varying the radius of the stars by $\pm$5 per cent (keeping other parameters constant).

calculations) results in $R_{\rm p}$ being overestimated by up to 50 per cent (Seager & Mallén-Ornelas 2003, fig. 12). Therefore, we deemed these candidates worthy of follow-up.

An inspection of Digitized Sky Survey images revealed that each of the candidates were affected by some level of blending in the APT photometry aperture.

We obtained higher spatial resolution images using the 40-inch telescope at SSO. We aimed to monitor each candidate continuously during a predicted transit, alternating between the *V* and *I* bands. To improve the time-sampling, we only read out one-quarter of the full CCD, corresponding to a 10-arcmin² field (sampled by 1k × 1k, 0.6-arcsec pixels). Due to a run of bad weather, we only observed one of the candidates (UNSW-TR-2) during a transit. In this case, the source of the transit signal is in fact the second bright star in the APT aperture ($\sim$0.8 mag fainter than the brightest one, and $\sim$10 arcsec from it). The undiluted light curve (Fig. 6) shows a V-shaped eclipse with a depth of 0.14 mag, suggesting that the signal is from a grazing eclipsing binary system.

Simultaneously with the high-resolution imaging, we obtained spectra using the Double-Beam Spectrograph (DBS) on the 2.3-m telescope, also at SSO. We used the highest-resolution grating in both arms. The approximate spectral ranges covered were 5700–6700 Å in the red arm and 3900–4400 Å in the blue, with resolutions of 1.1 Å (45 km s^{-1}) and 0.5 Å (40 km s^{-1}), respectively. We

Table 2. Transit candidates in the NGC 6633 field: coordinates and parameters estimated from APT data. $T_{\rm c}$ is the time at the centre of the first transit we detected (JD$-$2450000). Coordinates are from the WCS solution in the APT images, and represent the centroid (to within $\sim$1 arcsec) of the object, which is generally a blend. Similarly, the given *V* magnitudes, with errors of $\sim$0.1 mag, are for the blend as measured by the APT. Errors in the other measured parameters are 5 × 10^{-5} d for the period, 0.01 d for $T_{\rm c}$, 5 mmag for the transit depth (ΔF) and $\sim$0.5 h for $t_{\rm T}$ and $t_{\rm F}$ (the duration of the complete transit, and of the 'flat bottom' part, respectively). Estimates for the radius of the star (R_1) and the planet (R_2) were derived using the equations of Seager & Mallén-Ornelas (2003). UNSW-TR-1 is a member of the cluster (NGC 6633 141).

ID	RA (J2000)	Dec. (J2000)	V	P (d)	$T_{\rm c}$ (d)	ΔF (mmag)	$t_{\rm T}$ (h)	$t_{\rm F}$ (h)	R_1 ($R_\odot$)	R_2 ($R_{\rm Jup}$)
UNSW-TR-1	18 29 04.4	+06 26 54	11.0	2.38079	2496.93	30	3.4	2.0	1.4	2.9
UNSW-TR-2	18 30 51.9	+07 09 20	12.0	1.05837	2462.99	25	1.9	0.2	1.5	2.4
UNSW-TR-3	18 31 00.7	+07 08 25	13.0	1.81749	2499.07	70	2.0	0.5	0.8	2.0
UNSW-TR-4	18 32 22.3	+06 37 13	12.9	4.39995	2465.13	50	3.8	0.7	1.2	3.8

Table 3. Transit candidates in the NGC 6633 field: parameters obtained from follow-up spectroscopy. The error on the primary mass (M_1) was assumed to be 10 per cent. The velocity amplitude of TR-2 was estimated from the separation of double lines in the single spectrum we obtained. As it is a binary system with nearly identical components, the orbital period is twice the value measured from the APT light curves. We assumed the two stars have equal mass. The orbit of TR-4 appears to be eccentric, but we have insufficient data for a rigorous Keplerian fit. Assuming a circular orbit gives the result quoted here.

Star ID	Sp type	M_1 ($\mathrm{M_\odot}$)	K (km s^{-1})	M_2 ($\mathrm{M_\odot}$)
UNSW-TR-1	A2V	2.5	27 ± 3	0.34 ± 0.05
UNSW-TR-2	K7V	$=M_2$	87 ± 3	0.58 ± 0.05
UNSW-TR-3	F7V	1.2	53 ± 10	0.4 ± 0.1
UNSW-TR-4	F5V	1.3	~ 20	~ 0.2

measured the radial velocities by cross-correlating the H$_\alpha$ absorption line in each spectrum with a spectrum of the RV standard star β Vir (obtained with the same instrument).

We also obtained a single low-resolution (2.2 Å) spectrum of each object covering the range 3420–5350 Å. These were visually compared to templates from the UVILIB spectral library (Pickles 1998), yielding a spectral type estimate for each candidate (Table 3).

Due to the limited observing time, we were unable to monitor all stars blended within each APT photometry aperture. Therefore, we observed the brightest star in each aperture at several independent phases, and took single spectra of the fainter neighbouring stars. If the transits were in front of the fainter stars, they would be more likely to be of stellar origin (because the undiluted transit depth would have to be larger).

For three of the candidates (UNSW-TR-1, 3 and 4), the brightest star shows large RV variations in phase with the transit signal. The velocity semi-amplitude (K) of the candidates is shown in Table 3. The companion masses were calculated using an estimate of the primary's mass from its spectral type, and assuming circular orbits (which is consistent with the RV curve for two of these cases). Clearly the companions are low-mass stars, and not planets.

6.2.1 A K7Ve binary system

For the fourth candidate (UNSW-TR-2), the RV of the bright star dominating the light in the aperture showed no coherent variations when folded at the period measured from the transits. We only had one DBS spectrum of this star's close neighbour, which was revealed in the 40-inch images to be the source of the transit signal. This spectrum is well matched by a K7V template, with two important exceptions: (i) there is a strong H$_\alpha$ emission peak; (ii) the absorption lines and the emission line all have two components of approximately equal strength. Taking into account the orbital phase at the time the spectrum was taken, the maximum velocity separation between the components is 175 ± 6 km s^{-1}.

We were able to obtain two more spectra of this star at lower resolution. Although the double-line structure is not completely resolved in these spectra, they do confirm that the separation between the lines varies with orbital phase. We have not performed a rigorous fit to the light curves. However, a model consisting of two identical K7V stars, each of mass 0.58 ± 0.05 M$_\odot$ and radius 0.64 ± 0.01 R$_\odot$, appears to fit all the observations. The period is 2.11674 ± 0.00002 d (twice the original estimate), giving an orbital radius of ~ 0.03 au. The orbital inclination is $83.4° \pm 0.1°$.[4]

This system may be a valuable addition to the small number of known double-lined eclipsing binary systems with late-type components, for which the physical parameters can be measured with precision (e.g. Torres & Ribas 2002; Maceroni & Montalbán 2004; C. Maceroni, private communication). Such measurements provide important constraints for models of low-mass stars.

6.3 Variable stars

Visual inspection of the individual *V*-band light curves revealed the presence of 49 well-defined variable stars. Of these, three were previously known variable stars (HD 170451, BP Ser and BI Oph). We classified the remaining 46 following a simple procedure based on the period and the shape of the light curve. To minimize personal biases, we put stars into broad classes such as short-period pulsators or eclipsing binaries. For a few stars, we were able to determine the GCVS type unambiguously.

The following types of variables were found: 40 pulsating stars (33 short period, five RR Lyrae-type, two long-period semiregular) and nine eclipsing binaries. We found a number of bright short-period pulsating stars having A–F spectral types,[5] which suggests that they are likely δ Scuti stars. For the majority, however, the lack of spectroscopic observations prevents more detailed classification.

The period determination was performed using PERIOD98 of Sperl (1998) and the phase dispersion minimization method (Stellingwerf 1978). In addition to the frequencies, we also calculated S/N ratios in the Fourier spectra to obtain a measure of reliability of the determined frequencies. Following Breger et al. (1993), we adopted S/N > 4 as the limit of significance. The detected variable stars and their basic parameters (catalogue number, coordinates, period, type of variability) are listed in Table 4. Although in some cases there is evidence for multiple periodicity, this is beyond the scope of the present paper.

7 EXPECTED PLANET DETECTION RATE

7.1 A rough estimate

The number of detectable planets in our search can be approximated as

$$N_{\mathrm{det}} = N_{\mathrm{dwarf}} P_{\mathrm{pl}} P_{\mathrm{tr}} P_{\mathrm{obs}}, \qquad (5)$$

where N_{dwarf} is the number of dwarf stars in our fields for which a hot Jupiter would cause at least a 10-mmag transit, P_{pl} is the fraction of stars that actually host such a planet, P_{tr} is the geometric probability that the planet does transit (i.e. that it crosses our line of sight to the star) and P_{obs} is the probability that we observe multiple transits, with some minimum combined S/N ratio [$(S/N)_{\mathrm{min}} \approx 10$].

A typical transiting hot Jupiter, with radius $1.2\,R_{\mathrm{Jup}}$ (e.g. Sozzetti et al. 2004, Fig. 3), will cause at least a 10-mmag transit in front of any star with radius $R_* \leqslant 1.2\,\mathrm{R}_\odot$, i.e. of spectral type $\sim$F8 or later. For a magnitude-limited sample, $\sim$50 per cent of stars are of type GKM (Cox 2000). Thus, we have $N_{\mathrm{dwarf}} \approx 0.5\,N_*$, where N_* is the total number of stars monitored with at least 10-mmag precision (i.e. with $V \lesssim 13$). For the NGC 6633 field, $N_* \approx 2000$.

The frequency of hot Jupiters is $P_{\mathrm{pl}} \approx 1$ per cent (e.g. Gaudi, Seager & Mallén-Ornelas 2005), and their transit probability is $P_{\mathrm{tr}} \approx R_*/a \sim 0.1$ (where a is the orbital radius). Therefore, observing a rich Galactic field such as NGC 6633, we have

---

[4] The fitted radius and inclination are strongly correlated.

[5] Spectral types were obtained from the SIMBAD on-line catalogue.

Table 4. Variable stars found in the NGC 6633 field. As this is a relatively crowded field, most objects are blends. As a consequence: (i) the actual variable star may be another star within ~30 arcsec of the catalogue star we identify; (ii) the coordinates shown represent the centroid of the blend; (iii) the *V* magnitudes measure the total flux in the APT photometry aperture; (iv) the amplitudes may be diluted by blended stars, and thus the values shown are only approximate lower limits. Coordinates were calculated from the WCS solution in the APT images, with a precision of ~1 arcsec. The magnitude zero-point calibration is accurate to ~0.1 mag.

Id	Catalogue Id	RA (J2000) (^{h} ^{m} ^{s})	Dec. (J2000) ($^\circ$ $'$ $''$)	V	P (d)	A (mmag)	Type
V1		18 22 10.2	+6 23 20	12.9	0.09225	8	Short-period pulsator
V2		18 22 08.3	+6 42 42	13.2	0.78357	285	W UMa
V3	GSC 00445-00528	18 23 11.7	+6 18 53	10.1	0.13704	10	Short-period pulsator
V4		18 23 06.9	+6 42 13	12.3	0.14254	10	Short-period pulsator
V5	GSC 00445-00689	18 23 09.1	+6 51 35	10.6	0.19818	9	Short-period pulsator
V6		18 23 27.5	+6 12 06	12.8	0.09452	42	Short-period pulsator
V7		18 23 33.1	+6 33 29	12.8	0.38673	242	W UMa
V8		18 23 47.9	+7 28 05	12.4	1.02289	312	Algol
V9	GSC 00445-01888	18 23 42.5	+6 24 09	11.1	0.09855	10	Short-period pulsator
V10		18 24 27.1	+6 45 42	12.1	0.19167	13	Short-period pulsator
V11		18 24 32.6	+7 30 46	12.0	0.06285	5	Short-period pulsator
V12		18 24 40.2	+6 10 05	12.5	0.06559	42	Short-period pulsator
V13		18 24 45.2	+6 05 31	12.4	0.28535	153	RR Lyrae
V14	NGC 6633 8	18 24 40.6	+7 04 05	9.2	0.15436	38	Short-period pulsator
V15		18 25 14.8	+6 33 54	11.5	0.07567	6	Short-period pulsator
V16	NGC 6633 14	18 25 04.1	+6 25 55	10.0	0.03658	14	Short-period pulsator
V17		18 25 10.1	+6 46 44	11.6			Eclipsing binary
V18		18 26 14.4	+5 34 54	13.1	1.63336	185	Algol
V19		18 26 34.7	+6 06 19	13.0	0.28913	36	Short-period pulsator
V20		18 26 42.3	+7 05 02	11.2	0.05681	20	Short-period pulsator
V21		18 26 19.7	+7 27 58	12.2	0.14068	10	Short-period pulsator
V22		18 26 54.2	+6 58 06	11.8	0.14862	45	Short-period pulsator
V23	NGC 6633 54	18 26 44.9	+6 24 20	10.1	0.07472	4	Short-period pulsator
V24	NGC 6633 89	18 27 33.4	+6 56 00	10.7	0.06734	10	Short-period pulsator
V25		18 27 40.9	+7 08 34	11.4	0.05363	18	Short-period pulsator
V26	NGC 6633 108	18 28 04.0	+5 58 13	10.3	0.08375	5	Short-period pulsator
V27	GSC 00445-00634	18 27 53.3	+6 08 51	11.2	0.34196	25	RR Lyrae
V28	Cl* NGC 6633 VKP 188	18 28 24.4	+6 13 37	11.3	1.11068	17	Eclipsing binary
V29		18 28 57.3	+6 21 02	13.3	1.81161	253	Eclipsing binary
V30	NGC 6633 131	18 28 33.8	+6 53 15	10.0	0.04723	8	Short-period pulsator
V31	NGC 6633 135	18 28 42.9	+6 51 25	10.4	0.03634	6	Short-period pulsator
V32		18 29 10.2	+6 43 52	12.9	0.11138	24	Short-period pulsator
V33		18 28 58.0	+7 28 33	12.0	0.09568	188	Short-period pulsator
V34	NGC 6633 149	18 29 17.3	+5 39 20	10.8	0.04683	6	Short-period pulsator
V35	NGC 6633 147 (HD 170451)	18 29 12.8	+6 47 14	9.5	0.37532	355	W UMa
V36	V* BP Ser	18 30 13.4	+6 16 50	12.5			LB
V37		18 30 29.0	+5 48 39	12.8	0.04203	12	Short-period pulsator
V38	GSC 00458-01442	18 30 41.9	+6 47 50	10.9	0.31777	9	RR Lyrae
V39	GSC 00458-00757	18 30 59.8	+7 11 51	10.7	0.11008	4	Short-period pulsator
V40		18 31 02.4	+6 05 01	12.3	0.03941	7	Short-period pulsator
V41	V* BI Oph	18 31 07.6	+7 00 32	11.2	202.59		Mira Cet
V42		18 31 18.7	+7 05 25	12.7	0.07343	9	Short-period pulsator
V43		18 31 19.5	+7 26 21	13.3	0.53548	186	RR Lyrae
V44		18 31 59.2	+5 40 19	10.7	0.43263	122	RR Lyrae
V45		18 32 05.6	+7 14 56	11.9	0.05936	9	Short-period pulsator
V46		18 32 51.9	+6 49 01	13.3	0.50552	156	W UMa
V47		18 33 17.3	+5 58 31	12.2	0.21377	146	Pulsating
V48	GSC 00458-01108	18 33 16.4	+6 29 08	9.1	0.15686	6	Short-period pulsator
V49		18 34 03.5	+6 36 03	12.6	0.13636	12	Short-period pulsator

$N_{det} \approx P_{obs}$. For our complete NGC 6633 light curves, $P_{obs} \approx$ 0.4 (minimum one complete and one partial transit, $1 < P < 9$ d; see Fig. 7), giving an estimate of 0.4 planets for this data set, or ~0.2 planets per year.

In this simple estimate, we have made some gross simplifications, including

(i) neglecting the dependence of P_{pl}, P_{tr} and P_{obs} on the orbital period, and other properties of the star and planet;

(ii) assuming a very simple (and perhaps optimistic) dependence of the detection probability on the transit depth, and neglecting the distribution of transit depths among target systems;
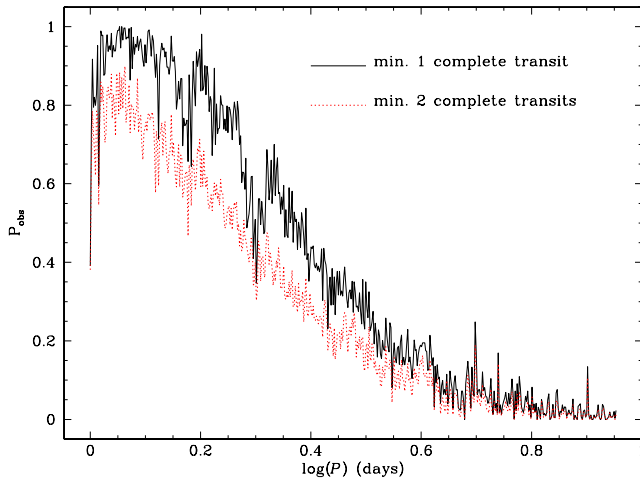
Figure 7. The probability of observing at least one (solid line) or two (dotted line) complete transits of a transiting planet in the light curves we have obtained for the NGC 6633 field. A minimum of 100 in-transit data points are required for a detection (so that 10-mmag precision yields a total S/N ratio of ≥10 for a typical transiting hot Jupiter). A typical transit duration of 0.1 day is assumed. The one-transit probability also includes the requirement of at least one additional partial transit, so that the period can be estimated. The mean probability over this period range (1–9 d, sampled logarithmically) is 0.4 for one transit, and 0.3 for two transits.

(iii) neglecting the three-dimensional distribution of stars in the Galactic disc;

(iv) neglecting interstellar extinction;

(v) neglecting the effect of blends in a crowded field;

(vi) ignoring the possible effects of stellar companions on detection probability (only ~1/3 of late-type dwarfs are single stars; Duquennoy & Mayor 1991).

Therefore, this is only an order-of-magnitude figure, but will provide a useful comparison to the results of our more detailed analysis.

We note that Horne (2003) estimates a detection rate of three planets per month for our project, using simple scaling laws. However, by his calculations, all the transit surveys combined should be detecting 191 planets each month, which is clearly an overestimate. The main goal of these calculations was perhaps not an estimate of the absolute detection rate, but rather a comparison of the various projects. If we assume the six planets found by the transit method to date were detected from a single year of observations by all the projects, and scale Horne's estimate to match this rate, then his estimate for our search becomes 0.09 planets per year. For a transit search with parameters comparable to ours (although a shorter observing run), Brown (2003) estimates a rate of ~0.7 detected planet per 10^4 stars monitored (to a magnitude limit of $R = 12$). Our estimate above translates to ~ two planets per 10^4 stars. Brown's analysis includes a number of effects, such as that of the planet period and radius distributions, which reduce the detection rate compared to our simple estimate.

7.2 Monte Carlo simulation

In order to obtain a more realistic estimate, we have modelled our observations using a Monte Carlo simulation. This allows us to use a realistic photometric noise model, and to take various observational effects into account (in particular blending, and the set of epochs at which the light curves are sampled).

We begin by simulating a population of stars in a 1 deg^2 field of view. We use the luminosity function for the Solar neighbourhood, $\Phi_0(M_V)$ (as tabulated in Cox 2000, for $M_V = -7, -6, \ldots 18$), allowing for an exponential drop-off with height above the Galactic plane (with scaleheights, $H(M_V)$, from Allen 1973). The number of stars of absolute magnitude M_V per cubic parsec, at a distance d and Galactic latitude b, is thus

$$\Phi(M_V, d, b) = \Phi_0(M_V)e^{-d|\sin b|/H(M_V)}. \tag{6}$$

We divide the volume sampled by a 1 deg^2 field into a series of shells of thickness 20 pc. We fill each shell with the appropriate number of stars in each M_V bin. To calculate the apparent (V) magnitude of each star, we assume an extinction of 1.9 mag kpc^{-1} in the Galactic plane, dropping off exponentially with distance from the plane, with a scaleheight of 140 pc (Allen 1973). Only stars with $5 < V < 19$ are included in the model, as stars brighter than this can be avoided during field selection, while fainter stars are not resolved in APT images.

Depending on M_V, an appropriate fraction of stars (tabulated in Cox 2000) are simulated as binary systems. For simplicity, a luminosity ratio is randomly selected from a uniform distribution in the range (0, 1).[6] The absolute magnitude of the primary is adjusted for this (keeping the total luminosity of the system equal to the original M_V), and the secondary is ignored.

Apart from binary companions, a three-pixel radius photometry aperture centred on a star in an APT image typically includes light from several other stars. We randomly assign pixel coordinates to the simulated stars, within a section of the APT CCD corresponding to 1 deg^2. For each star, we then calculate what fraction of the total starlight in the aperture comes from that star, and we take this into account when calculating the observed transit depth due to a planet. Stars for which this fraction is less than 5 per cent are excluded from further analysis, as any planetary transit signal from these stars would be diluted below our detection limit.

Around each remaining star, we place a planet with a radius of $R_p = 1.2 R_{Jup}$. We randomly select a period in the range 1–9 d, using the distribution described by Gaudi et al. (2005): uniform in $\log P$ in each of two bins, 1–3 d ['very hot Jupiters' (VHJs)] and 3–9 d ['hot Jupiters' (HJ)], with the frequency of VHJ relative to HJ being 15 per cent.

Tables in Lang (1992) give the mass (M_*) and radius (R_*) of the star based on its absolute magnitude, assuming it is on the main sequence. For the planet, we assume a circular orbit, with radius $a = (1\,\mathrm{au})(M_*/M_\odot)^{1/3}[P/(1\,\mathrm{yr})]^{2/3}$. We then randomly select an orbital inclination (i) leading to a transit (i.e. select $\cos i$ from a uniform distribution in the range 0–P_{tr}, where $P_{tr} \approx R_*/a$ is the probability of such an inclination for a randomly oriented orbit).

Neglecting limb-darkening, grazing transits and ingress/egress times, we approximate the signal as a rectangular transit of depth $\Delta F = (R_p/R_*)^2$, and duration

$$\Delta t = \frac{P}{\pi a}\sqrt{(R_* + R_p)^2 - (a\cos i)^2}. \tag{7}$$

We assume that we will reliably detect planets with $\Delta F > \Delta F_{min} = $ 10 mmag, provided multiple transits are observed and a minimum

---

[6] The observed distribution of binary mass ratios peaks near $q = 0.3$ and drops off considerably at higher values (Duquennoy & Mayor 1991). Therefore, on average, our simplification overestimates the dilution of the primary's light by the companion, leading to a slightly lower estimate of the probability of detecting a planet around the primary.

total S/N ratio is reached [$(S/N)_{min} = 10$]. Considering that the light curves we have obtained to date frequently contain systematic trends of the order of 10 mmag, this value of ΔF_{min} is somewhat optimistic. For our present analysis of the NGC 6633 light curves, a value of 20 mmag would be more realistic. Well-sampled transits of that depth (superimposed on the systematics) are easily detectable, at least by visual inspection. However, we are confident that our implementation of the Kovács et al. (2004) trend filtering algorithm, combined with transit detection software, will allow us to reliably detect transits as shallow as 10 mmag (Section 5.4). Thus, we will continue to use this optimistic value for ΔF_{min}, while noting that it is an important parameter. Its effect on the planet catch is discussed below.

We estimate the photometric precision per measurement using a noise model which includes Poisson noise due to star and sky flux, and a limiting precision of 1.5 mmag for the bright stars (the solid curve in Fig. 4). Combined with ΔF, this tells us the number of in-transit measurements (N_{min}) that need to be made in order to achieve a total S/N ratio $(S/N)_{min}$. Given a simulated planet and a set of observation epochs, we can calculate the probability (P_{obs}) that a minimum of two complete transits will be observed, including at least N_{min} in-transit points. We do this by testing 1000 transit epochs.

To estimate the total planet catch for the assumed observing parameters (Galactic latitude and observation epochs), we add up the values of $P_{tr} \times P_{obs}$ for each simulated planet, and scale the result to the appropriate field size. We also multiply by the fraction of stars that do host short-period planets, which is ~1 per cent (e.g. Gaudi et al. 2005).

7.3 Validating the simulation

In order to ensure that this rather complicated simulation yields reasonable results, we performed a number of tests. First, we generated a set of fake APT images using the distribution of stars from the simulation (for $b \approx 8°$). The simulated images appear very similar to a real image at the same Galactic latitude (with the exception of some patches of increased extinction in the real image). Processing these fake images through the photometry pipeline, we also confirmed that the star counts as a function of limiting magnitude closely match those obtained from a real image.

We then modified the simulation to reproduce the simplifying assumptions made by Horne (2003). The result was within a factor of 2 of Horne's estimate for our project. Finally, we confirmed that the result scales with planet, star and observational parameters (R_p, a, M_V, R_*, sky brightness, survey duration and $(S/N)_{min}$) as predicted by Horne's equation 3.

7.4 Results for the NGC 6633 field

We have simulated observations at the Galactic latitude of our NGC 6633 field ($b = 8°$), using the epochs of the best images we have obtained for this field in 2002–2004 (2486 images, from 61 nights over three seasons). The expected planet catch for a single 6-deg^2 APT field is ~0.1 planet ($\Delta F_{min} = 10$ mmag, two complete transits). If we accept one complete observed transit as a detection (plus at least one partial transit so that some estimate of the period can be made), the estimate becomes ~0.2 planet, which agrees well with the rough estimate derived in Section 7.1.

As expected, we are most sensitive to planets with the shortest periods (Fig. 8). However, because we have simulated planets with
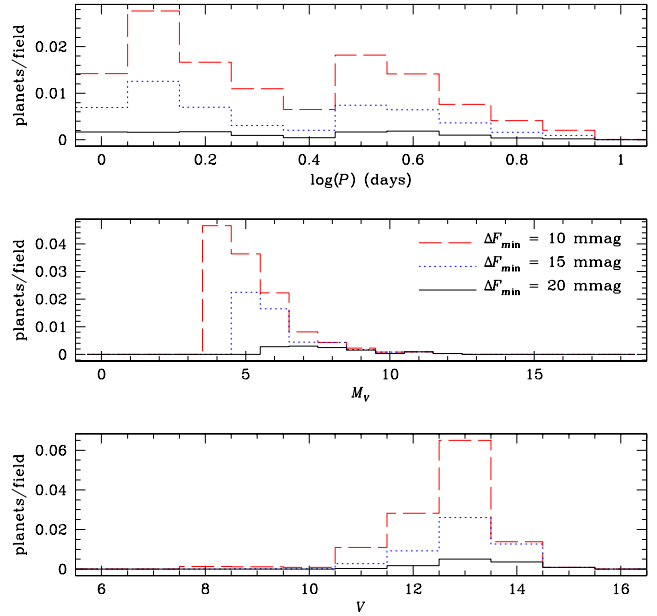

Figure 8. Distribution of period (top panel), host star absolute magnitude (middle panel) and apparent magnitude (bottom panel) for detected extrasolar planets in the Monte Carlo simulation. The histograms were generated by weighting each simulated planet by the probability of detecting it ($P_{tr} P_{obs}$). The simulation parameters were set to match those of our observations of the NGC 6633 field in 2002–2004. In each panel we show the distribution for three different values of the minimum detectable transit depth.

Table 5. The total number of detected planets per APT field (minimum two complete observed transits) as a function of the minimum detectable transit depth (ΔF_{min}, given in the first row in mmag). We compare two simulations: our NGC 6633 observations (2002–2004, V band, Section 6.1) and higher-cadence observations at a Galactic latitude of 25° in the I band over two months (Section 7.5).

Strategy	10	15	20	30
NGC 6633 obs.	0.12	0.05	0.01	0.004
New strategy	0.20	0.12	0.08	0.050

periods longer than 3 d to be almost 10 times more frequent than those with $P < 3$ d (according to the observed distribution), the distribution of detected planets also has a peak at 3–5 d. Most detected planet hosts have an apparent magnitude $V \approx 13$, while almost none are fainter than $V \approx 14.5$.

The luminosity distribution of detected host stars peaks at $M_V \approx 4$ (for $\Delta F_{min} = 10$ mmag), as also predicted by Pepper, Gould & Depoy (2003). Amongst the stars that are small enough for a 1.2-R_{Jup} planet to cause a 10 mmag transit, those with $M_V \approx 4$ are the brightest and therefore the most numerous in our magnitude-limited sample. As a result, ΔF_{min} is perhaps the most important parameter in determining the total planet catch.[7] In the case of the NGC 6633 data set, about 90 per cent of the systems detected with $\Delta F_{min} = 10$ mmag have transits shallower than 20 mmag (Table 5).

---

[7] The largest detectable host-star radius is $\Delta F_{min}^{-1/2} R_p$. Varying the assumed planet size (R_p) is equivalent to varying $\Delta F_{min}^{-1/2}$.

This highlights the importance of removing systematic trends from our light curves so that shallow signals can be detected.

Repeating the simulation for one of the other seven fields (for each of which we have ∼1000 useful images, over two seasons) gives 0.03 planets per field (ΔF_{min} = 10 mmag, two complete transits). The reduced estimate compared to the NGC 6633 field is due to the smaller number of images, fewer nights with long continuous coverage (mostly due to bad weather), and sparser time-sampling. Thus, our most optimistic estimate of the planet catch in the data we collected over 2002–2004 is ∼0.3 planets, or ∼0.6 if we settle for one complete transit.

7.5 Discussion

The above disappointing estimate suggests that our initial strategy of simultaneously monitoring four fields over multiple seasons is far from optimal. We selected this strategy believing it would maximize the number of stars we monitor, while obtaining a minimum time-sampling required to detect a transit (one image every ∼14 min). The S/N ratio of a detection would be increased by folding the light curve at the appropriate period. However, gaps in the observations due to weather and technical problems have reduced the probability of detecting multiple, complete transits (Fig. 7). To date, the systematic trends present in many light curves have prevented the use of detection software to make shallow transits detectable by phase-folding. We need to sample the light curves more frequently so that the required total S/N ratio can be accumulated over a small number of observed transits.

We have used the Monte Carlo simulations to study the effects of various observational parameters on the planet catch, and thus select a more efficient search strategy. One important change was the choice of filter. Other transit-search teams have discussed the merits of observing at long wavelengths, in particular in the *I* band (e.g. von Braun et al. 2005). In terms of maximizing the detection rate, there are two main advantages. First, the greater CCD sensitivity in the *I* band allows shorter exposures (60 s, compared to 150 s in *V*) and thus higher-cadence observations. Secondly, observing in the *I* band significantly increases the number of well-measured red dwarf stars in our sample (which have deeper transits) relative to their larger, bluer counterparts. This makes the total detection rate less sensitive to the minimum detectable transit depth (see Table 5 and Fig. 9).

The simulations indicate that the detection rate is essentially constant from the Galactic plane out to a latitude of $|b| \approx 25°$, and is only reduced by ∼20 per cent even at $|b| \approx 65°$. This is due to the reduced blending in less crowded fields, as well as the near-isotropic distribution of the well-measured red stars (most of which are within ∼100 pc). Although we have not calculated the frequency of 'false positive' detections due to eclipsing binaries blended with a third star along the line of sight, this will be significantly lower in the higher latitude fields. Furthermore, the photometric precision (and absence of systematics) we have assumed in the simulation are easier to achieve in less crowded fields. For these reasons we conclude that fields in the range $15° \lesssim |b| \lesssim 45°$ are optimal.

Future fields will be at southern declinations, so that they are observable at low airmass for a full 8 h every night.[8] We will select pairs of adjacent fields, obtaining an image of each field every 4 min.

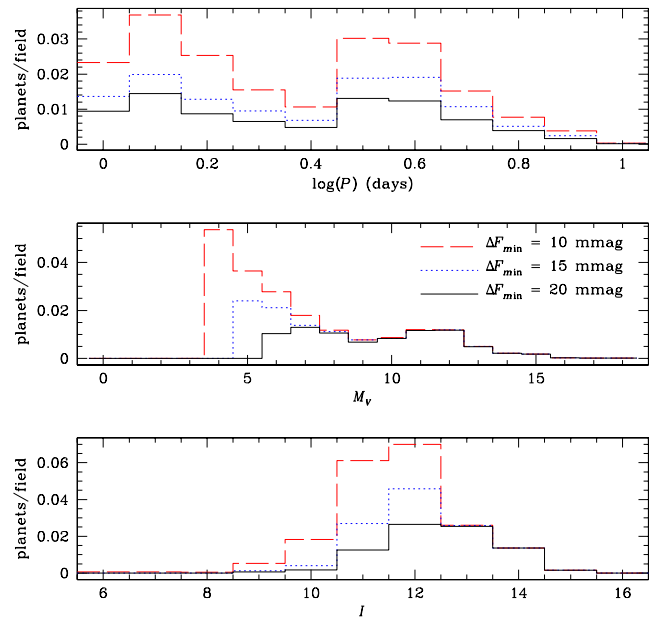[8] From SSO, we have a minimum of 8 h of darkness per night for eight months each year.

Figure 9. Distribution of the properties of detected systems for a model of our optimal observing strategy. Compare to Fig. 8, representing our initial strategy. We are confident that with future improvements in our trend filtering and detection software, the ΔF_{min} = 10 mmag case will become a realistic one.

We have simulated this new strategy, taking into account the different stellar magnitudes, lower interstellar extinction and brighter sky in the *I* band. We can achieve a detection rate of 0.2 planet per field (ΔF_{min} = 10 mmag, two complete transits) in only 20 nights of observations (taken over up to two months, allowing for gaps due to bad weather and full Moon).

Observing 10 fields per year (one pair for every two months, allowing for telescope downtime) will lead to an overall detection rate of two planets per year, a significant improvement over the estimated 0.2–0.3 yr^{-1} for our 2002–2004 observations. If further efforts do not allow us to reliably detect transits shallower than 20 mmag, the estimate for the new strategy is halved, while for the past observations it is reduced by a factor of 10 (Table 5).

8 CONCLUSIONS

We have described in detail the methods we have used to achieve mmag-precision relative photometry using the APT. For bright stars, the precision was limited by intrapixel variations in CCD sensitivity (IPSV), coupled with undersampling of the images. This was largely overcome by a new observing technique, which optimally alters the effective PSF in order to average out the effects of IPSV. We have demonstrated that using this technique, a customized aperture photometry package and an automated processing pipeline, we can obtain the large number of high-quality light curves required to detect transiting extrasolar planets.

During 2002–2004, we observed eight fields near the Galactic plane. Our analysis of data from the field centred on the open cluster NGC 6633 yielded four transit candidates. Follow-up observations revealed each of these to be eclipsing binary systems. We also found 49 variable stars in this field. Three of the other fields also contained binary stars with eclipses similar to those of a transiting planet.

By simulating the population of stars we observe, the properties of the telescope and our observing strategy, we have studied

the sensitivity of our search to short-period planets. Assuming the frequency of planets around stars targeted by RV surveys is representative of the Galactic field stars we observe, we have estimated our expected detection rate. Considering all the good-quality light curves for the eight fields we have observed to date, we expect to find 0.3–0.6 planets.

Our new strategy, whereby we obtain high-cadence observations in the *I* band, will yield an estimated two planets per year, a tenfold increase in detection rate over previous observations. We have been using this strategy since 2004 November. The new camera for the APT, being built in 2005, will have at least three times the field of view of the current one, higher sensitivity and smaller pixels. This will further increase the detection rate by a factor of a few.

REFERENCES

Aigrain S., Irwin M., 2004, MNRAS, 350, 331
Allen C. W., 1973, Astrophysical Quantities, 3rd edn. Athlone Press, London
Alonso R. et al., 2004, ApJ, 613, L153
Anderson J., King I. R., 2000, PASP, 112, 1360
Artymowicz P., Lubow S. H., 1994, ApJ, 421, 651
Bakos G., Noyes R. W., Kovács G., Stanek K. Z., Sasselov D. D., Domsa I., 2004, PASP, 116, 266
Barnes J. W., Fortney J. J., 2004, ApJ, 616, 1193
Borucki W. J. et al., 2003, in Deming D., Seager S., eds, ASP Conf. Ser. Vol. 294, Scientific Frontiers in Research on Extrasolar Planets. Astron. Soc. Pac., San Francisco, p. 427
Bouchy F., Pont F., Santos N. C., Melo C., Mayor M., Queloz D., Udry S., 2004, A&A, 421, L13
Breger M. et al., 1993, A&A, 271, 482
Brown T. M., 2001, ApJ, 553, 1006
Brown T. M., 2003, ApJ, 593, L125
Brown T. M., Charbonneau D., Gilliland R. L., Noyes R. W., Burrows A., 2001, ApJ, 552, 699
Butler R. P., Marcy G. W., Vogt S. S., Fischer D. A., Henry G. W., Laughlin G., Wright J. T., 2003, ApJ, 582, 455
Carter B. D., Ashley M. C. B., Sun Y-S., Storey J. W. V., 1992, Proc. Astron. Soc. Australia, 10, 74
Charbonneau D., Brown T. M., Latham D. W., Mayor M., 2000, ApJ, 529, L45
Charbonneau D., Brown T. M., Noyes R. W., Gilliland R. L., 2002, ApJ, 568, 377
Correia A. C. M., Udry S., Mayor M., Laskar J., Naef D., Pepe P., Queloz D., Santos N. C., 2004, preprint (astro-ph/0411512)

Cox A. N., ed. 2000, Allen's Astrophysical Quantities, 4th edn. Springer, New York
Deeg H. J., 2002, in Foing B., Battrick B., eds, ESA SP-514, Earth-like Planets and Moons. ESA Publications Division, Noordwijk, p. 237
Doyle L. R., Deeg H., 2004, in Norris R., Stootman F., eds, Proc. IAU Symp. 213, Bioastronomy 2002: Life Among the Stars. Kluwer, Dordrecht, p. 80
Drake A. J., Cook K. H., 2004, ApJ, 604, 379
Duquennoy A., Mayor M., 1991, A&A, 248, 485
Gaudi B. S., Seager S., Mallén-Ornelas G., 2005, ApJ, 623, 472
Gilliland R. L. et al., 2000, ApJ, 545, L47
Henry G. W., Marcy G. W., Butler R. P., Vogt S. S., 2000, ApJ, 529, L41
Hidas M. G., Webb J. K., Ashley M. C. B., Lineweaver C. H., Anderson J., Irwin M., 2003, in Deming D., Seager S., eds, ASP Conf. Ser. Vol. 294, Scientific Frontiers in Research on Extrasolar Planets. Astron. Soc. Pac., San Francisco, p. 383
Hidas M. G., Webb J. K., Ashley M. C. B., Lineweaver C. H., Anderson J., Irwin M., 2004, in Norris R., Stootman F., eds, Proc. IAU Symp. 213, Bioastronomy 2002: Life Among the Stars. Kluwer, Dordrecht, p. 77
Høg E. et al., 2000, A&A, 355, L27
Holman M. J., Wiegert P. A., 1999, AJ, 117, 621
Horne K., 2003, in Deming D., Seager S., eds, ASP Conf. Ser. Vol. 294, Scientific Frontiers in Research on Extrasolar Planets. Astron. Soc. Pac., San Francisco, p. 361
Hui L., Seager S., 2002, ApJ, 572, 540
Irwin M., 1997, in Espinosa J., ed., 7th Canary Islands Winter School, Detectors and Data Analysis Techniques for Wide Field Optical Imaging. Cambridge University Press, Cambridge
Irwin M., Lewis J., 2001, New Astron. Rev., 45, 105
Jeffries R. D., 1997, MNRAS, 292, 177
Kjeldsen H., Frandsen S., 1992, PASP, 104, 413
Koelbloed D., 1959, Bull. Astron. Inst. Netherlands, 14, 265
Konacki M., Torres G., Jha S., Sasselov D. D., 2003, Nat, 421, 507
Konacki M., Torres G., Sasselov D. D., Jha S., 2005, ApJ, accepted (astro-ph/0412400)
Kovács G., Bakos G., Noyes R. W., 2004, MNRAS, 356, 557
Kruszewski A., Semeniuk I., 2003, Acta Astron., 53, 241
Lang K. R., 1992, Astrophysical Data I. Planets and Stars. Springer-Verlag, Berlin
Lauer T. R., 1999, PASP, 111, 1434
Maceroni C., Montalbán J., 2004, A&A, 426, 577
Martín S. et al., 2004, in Favata F., Aigrain S., Wilson A., eds, ESA SP-538, Second Eddington Workshop: Stellar Structure and Habitable Planet Finding. ESA Publications Division, Noordwijk, p. 349
Mayor M., Queloz D., 1995, Nat, 378, 355
Mazeh T. et al., 2000, ApJ, 532, L55
Mochejska B. J., Stanek K. Z., Sasselov D. D., Szentgyorgyi A. H., Westover M., Winn J. N., 2004, AJ, 128, 312
Naylor T., 1998, MNRAS, 296, 339
Pepe F. et al., 2004, A&A, 423, 385
Pepper J., Gould A., Depoy D. L., 2003, Acta Astron., 53, 213
Pickles A. J., 1998, PASP, 110, 863
Pont F., Bouchy F., Queloz D., Santos N. C., Melo C., Mayor M., Udry S., 2004, A&A, 426, L15
Raymond S. N., Quinn T., Lunine J. I., 2004, preprint (astro-ph/0407620)
Richardson L. J., Deming D., Wiedemann G., Goukenleuque C., Steyert D., Harrington J., Esposito L. W., 2003, ApJ, 584, 1053
Roxburgh I., Favata F., 2003, Astrophys. Space Sci., 284, 17
Schneider J., 1994, Astrophys. Space Sci., 212, 321
Seager S., Hui L., 2002, ApJ, 574, 1004
Seager S., Mallén-Ornelas G., 2003, ApJ, 585, 1038
Seager S., Sasselov D. D., 2000, ApJ, 537, 916
Sozzetti A. et al., 2004, ApJ, 616, L167
Sperl M., 1998, Comm. Asteroseis., 111, 1
Stellingwerf R. F., 1978, ApJ, 224, 953
Tinney C. G., Butler R. P., Marcy G. W., Jones H. R. A., Penny A. J., McCarthy C., Carter B. D., Bond J., 2003, ApJ, 587, 423
Torres G., Ribas I., 2002, ApJ, 567, 1140

Toyozumi H., Ashley M. C. B. 2005, PASA, submitted

Udalski A. et al. 2002a, Acta Astron., 52, 1

Udalski A., Szewczyk O., Zebrun K., Pietrzynski G., Szymanski M., Kubiak M., Soszynski I., Wyrzykowski L., 2002b, Acta Astron., 52, 317

Udalski A., Zebrun K., Szymanski M., Kubiak M., Soszynski I., Szewczyk O., Wyrzykowski L., Pietrzynski G., 2002c, Acta Astron., 52, 115

Udalski A., Pietrzynski G., Szymanski M., Kubiak M., Zebrun K., Soszynski I., Szewczyk O., Wyrzykowski L., 2003, Acta Astron., 53, 133

Vidal-Madjar A., Lecavelier des Etangs A., Désert J.-M., Ballester G. E., Ferlet R., Hébrard G., Mayor M., 2003, Nat, 422, 143

Vidal-Madjar A. et al., 2004, ApJ, 604, L69

von Braun K., Lee B. L., Seager S., Yee H. K. C., Mallén-Ornelas G., Gladders M. D., 2005, PASP, 117, 141

Webb J. K., Wormleaton I., 2001, PASA, 18, 252

Weldrake D. T. F., Sackett P. D., Bridges T. J., Freeman K. C., 2005, ApJ, 620, 1043

This paper has been typeset from a T_EX/L^AT_EX file prepared by the author.